HEALTH AND MEDICINE

Paramagnetic susceptibility measured by magnetic resonance imaging as an in vivo biomarker for iron pathology in epilepsy

Zhenghao Li[1]†, Qiangqiang Liu[2,3]†, Tongtong Xu[1], Ming Zhang[1], Li Li[1], Zhangpeng Chen[4], Yaohui Tang[1], Li Jiang[5], Yong Lu[6], Fuhua Yan[6], Yuyao Zhang[7], Jiwen Xu[2,3]*, Hongjiang Wei[1,8]*

Epilepsy, a neurological disorder marked by recurrent, unprovoked seizures, is often linked to dysregulated iron metabolism, resulting in iron overload and subsequent cellular dysfunction or death within epileptogenic regions. We proposed a specific, noninvasive technique using paramagnetic susceptibility imaging via magnetic resonance imaging to quantify in vivo brain iron levels, aiming to enhance our understanding of epilepsy pathology and improve diagnostic accuracy. Our imaging and histopathological studies demonstrated that paramagnetic susceptibility is a sensitive biomarker for iron quantification in epilepsy. This method effectively detects iron abnormality from various causes and highlights that iron alters within epileptogenic zones, indicating the presence of potentially salvageable tissue. Furthermore, iron accumulation was observed to disrupt cortical laminar structures in epileptogenic zones and was associated with the proliferation of central nervous system cells, particularly astrocytes. Paramagnetic susceptibility imaging provides previously unknown insights into epilepsy, offering potential applications in diagnostics, monitoring, and personalized treatment strategies.

INTRODUCTION

Epilepsy is one of the most prevalent and critical neurological disorders, characterized by recurrent and unprovoked seizures because of abnormal neuronal activity. This condition affects individuals of all ages and can lead to loss of consciousness, convulsions, or altered behavior (*1*, *2*). The etiology of epilepsy is highly complex (*3*, *4*), but substantial evidence indicates that iron, an essential trace element in the central nervous system (CNS), plays an important role in its pathophysiology by contributing directly or indirectly to seizure activity across diverse etiologies (*5*–*10*). For example, in experimental animal models, intracortical injection of iron and intracerebral hemorrhage following stroke or neurotrauma can trigger epileptic seizures. Iron leakage, often because of increased blood-brain barrier permeability in epilepsy, manifests in forms such as hemosiderin, ferritin, and hemoglobin (*11*, *12*). Dysregulated iron metabolism is tightly linked to oxidative stress, a hallmark of various structural (*13*), genetic (*14*), or immune-related epilepsies (*4*, *15*, *16*). This oxidative stress exacerbates CNS cell dysfunction and damage, leading to iron overload and ferroptosis (*11*, *13*, *17*). Iron overload also promotes lipid peroxidation, impairing protein function, and is associated with increased extracellular glutamate, which can result in the redistribution of iron between cortical and subcortical structures (*18*). Moreover, iron-mediated epilepsy could be mitigated pharmacologically through the attenuation of iron accumulation, ferritin alteration, and oxidative damage (*19*). Therefore, precise iron quantification could be a valuable target for diagnosis, monitoring, and personalizing treatment for epilepsy.

Given the critical role of iron in epilepsy, developing a specific and noninvasive technique for in vivo iron mapping is essential. Now, pathological biopsy is the gold standard for evaluating iron overload, but it is invasive and complicated to perform. Magnetic resonance imaging (MRI) offers excellent contrast and high-resolution images of biological tissues, providing comprehensive in vivo information. However, the behavior of paramagnetic iron in MRI signals is complex, primarily affecting the magnetic resonance (MR) signal by perturbing the B_0 field, which manifests as changes in the MRI signal phase (*20*, *21*). Techniques using these properties, like susceptibility-weighted imaging, R_2* relaxation rate, and more recently developed quantitative susceptibility mapping (QSM) (*11*, *22*–*27*), have been attempted to quantify iron in epilepsy, but these methods lack specificity because of interference from other magnetic substances in brain tissues (*28*, *29*), resulting in low sensitivity and specificity for clinical iron detection.

Accurate iron mapping requires the ability and sensitivity to detect iron and distinguish its effects from those of other substances, such as myelin and calcium (*30*). Magnetic susceptibility is an intrinsic tissue property that quantifies how a material's magnetization responds to an external magnetic field, a characteristic that can be measured using MRI (*31*). Paramagnetic materials, like iron, affect MRI signal dephasing, while diamagnetic materials exert their effects in the opposite direction. Iron, the most predominant source of paramagnetic susceptibility in brain tissues, exacerbates the dephasing of magnetization, directly leading to signal magnitude decay and accelerated phase accumulation with increased echo time (*32*). By modeling iron's unique effects on MR signals, it is possible to isolate the contribution of paramagnetic susceptibility from other diamagnetic substances (*33*–*35*). Thus, paramagnetic susceptibility mapping offers opportunities for precise iron imaging in the brain.

[1]School of Biomedical Engineering, Shanghai Jiao Tong University, Shanghai, China. [2]Department of Neurosurgery, Clinical Neuroscience Center Comprehensive Epilepsy Unit, Ruijin Hospital, Shanghai Jiao Tong University School of Medicine, Shanghai, China. [3]Clinical Neuroscience Center, Ruijin Hospital Luwan Branch, Shanghai Jiao Tong University School of Medicine, Shanghai, China. [4]Songjiang Research Institute, Shanghai Jiao Tong University School of Medicine, Shanghai, China. [5]Instrumental Analysis Center, Shanghai Jiao Tong University, Shanghai, China. [6]Department of Radiology, Ruijin Hospital, Shanghai Jiao Tong University School of Medicine, Shanghai, China. [7]School of Information Science and Technology, ShanghaiTech University, Shanghai, China. [8]National Engineering Research Center of Advanced Magnetic Resonance Technologies for Diagnosis and Therapy (NERC-AMRT), Shanghai Jiao Tong University, Shanghai, China.
*Corresponding author. Email: hongjiang.wei@sjtu.edu.cn (H.W.); xjw88@vip.163.com (J.X.).
†These authors contributed equally to this work.

Our previous work demonstrated that sensitive and specific iron quantification is feasible using gradient echo MRI by a subvoxel QSM technique (*35*).

In this work, we used the quantitative paramagnetic susceptibility (χ_{para}) obtained from the subvoxel QSM technique to measure changes in brain iron (*35*). We demonstrated that χ_{para} is a noninvasive, specific, and accurate biomarker of iron concentration in epilepsy. Our measurements of χ_{para} in patients revealed iron overload of diverse etiologies and showed that χ_{para} values correlate with the pathological severity of epilepsy foci. Ex vivo experiments on resected tissues from patients confirmed that χ_{para} maps effectively quantify iron overload in epileptogenic zones in vivo. We found that iron is concentrated in more localized tissue regions rather than being uniformly distributed across whole specimens. Cortical depth-wise analysis, both in vivo and ex vivo, confirmed that iron accumulation disrupts the normal layer-specific microstructure of epileptogenic zones and is associated with the proliferation of CNS cells, particularly astrocytes. In addition, we evaluated the effectiveness of χ_{para} in classifying different types of epilepsy, finding that it was able to further differentiate between subtypes on the basis of patterns of iron overload or deficiency. These findings indicated that iron detection and quantification using MRI-based paramagnetic susceptibility mapping could provide previous unknown insights into studying the epileptic brain.

RESULTS

Demographic and clinical characterization of patients with epilepsy

To comprehensively investigate iron overload in epilepsy, we recruited 156 refractory patients with epilepsy (66 females) and diverse disease manifestations from May 2021 to November 2024. All patients underwent clinical MRI scans, and positron emission tomography (PET) scans were performed on the basis of individual clinical assessments. Patients were classified into six groups according to imaging and pathological findings, with an additional group for those with unclear clinical pathogenesis (Table 1). As anticipated, nearly half of the patients (71 of 156, 45.5%) had negative results on conventional MRI scans. In our cohort, 39 patients underwent resection surgery, with a significant difference in the proportion of surgeries among each group ($P < 0.001$), suggesting that seizure severity varies with the underlying causes.

Iron-related epilepsy revealed by the paramagnetic susceptibility imaging

In this study, we demonstrated the sensitivity of paramagnetic susceptibility in identifying iron-related epileptogenic zones and its effectiveness in quantifying iron. Quantitative paramagnetic susceptibility imaging was calculated retrospectively, as well as R_2* maps and QSM maps, which are conventional techniques used for iron quantification. We used the paramagnetic susceptibility of tissue in the contralateral hemisphere corresponding to the epileptogenic zone as an individual reference. Hyperparamagnetic susceptibility (hyper-χ_{para}) in epileptogenic zones is defined as a higher value relative to that of the contralateral tissue. Hyperparamagnetic susceptibilities were observed in the clinically diagnosed epileptogenic zones of patients across all categories, with a substantial proportion (56 of 156, 35.9%) displaying these characteristics (Table 1).

Patients with traumatic injury, tumors, or vascular disease predominantly demonstrated hyperparamagnetic susceptibilities, while other patient categories showed these features to a lesser extent ($P < 0.001$, Table 1). For patients with abnormal brain development, such as focal cortical dysplasia (FCD) or cerebral atrophy sclerosis, T1-weighted (T1-w) and T2 fluid-attenuated inversion recovery (T2-FLAIR) images were useful in identifying morphological changes. However, clear lesions were not visually observed in these modalities or R_2* maps for this subset of patients (Fig. 1A). In contrast, abnormal hyperparamagnetic susceptibility was evident in these patients with low fluorine-18-fluorodeoxyglucose (^{18}F-FDG) uptake, as highlighted by yellow arrows. Both QSM images and χ_{para} maps showed hyperintensity. However, traditional QSM images (categorized as QSM > 0 and QSM < 0)

Table 1. Demographic and clinical information of patients with epilepsy. Hyper-χ_{para}, higher paramagnetic susceptibility of epileptogenic zones relative to that of the contralateral tissues.

Diagnosis	FCD (*n* = 25)	Traumatic injury (*n* = 18)	Atrophy and sclerosis (*n* = 19)	Tumor (*n* = 8)	Vascular disease (*n* = 6)	Other (*n* = 9)	Not clear (*n* = 71)	*P* value
Population of all patients (%)	16.0	11.5	12.2	5.1	3.8	5.8	45.5	
Sex (female/male)	11/14	8/10	8/11	2/6	2/4	4/5	31/40	0.971
Age (year)	21.2 ± 12.3	25.1 ± 12.5	26.2 ± 15.9	25.5 ± 14.3	43.7 ± 12.5	19.1 ± 13.6	22.0 ± 14.8	0.222
Age of first seizure (year)	9.8 ± 9.2	17.1 ± 11.2	10.1 ± 10.6	16.9 ± 12.9	26.3 ± 7.2	12.1 ± 12.2	13.5 ± 11.9	0.998
Duration of epilepsy (year)	11.4 ± 9.0	8.0 ± 8.3	16.1 ± 14.5	8.6 ± 7.8	17.3 ± 17.7	7.0 ± 7.9	8.5 ± 9.4	0.089
Resection	19 (76.0)	1 (5.6)	3 (15.8)	7 (87.5)	5 (83.3)	0 (0)	4 (5.6)	<0.001
Seizure side (left/right)								0.123
Left hemisphere	13	6	6	6	3	3	–	
Right hemisphere	11	8	6	2	2	5	–	
Both side	1	4	7	0	1	1	–	
Abnormal susceptibility distribution								<0.001
Hyper-χ_{para}	7 (28.0)	16 (88.9)	3 (15.8)	7 (87.5)	5 (83.3)	4 (44.4)	14 (19.7)	
Non–hyper-χ_{para}	5 (20.0)	0 (0)	3 (15.8)	0 (0)	0 (0)	0 (0)	3 (4.2)	

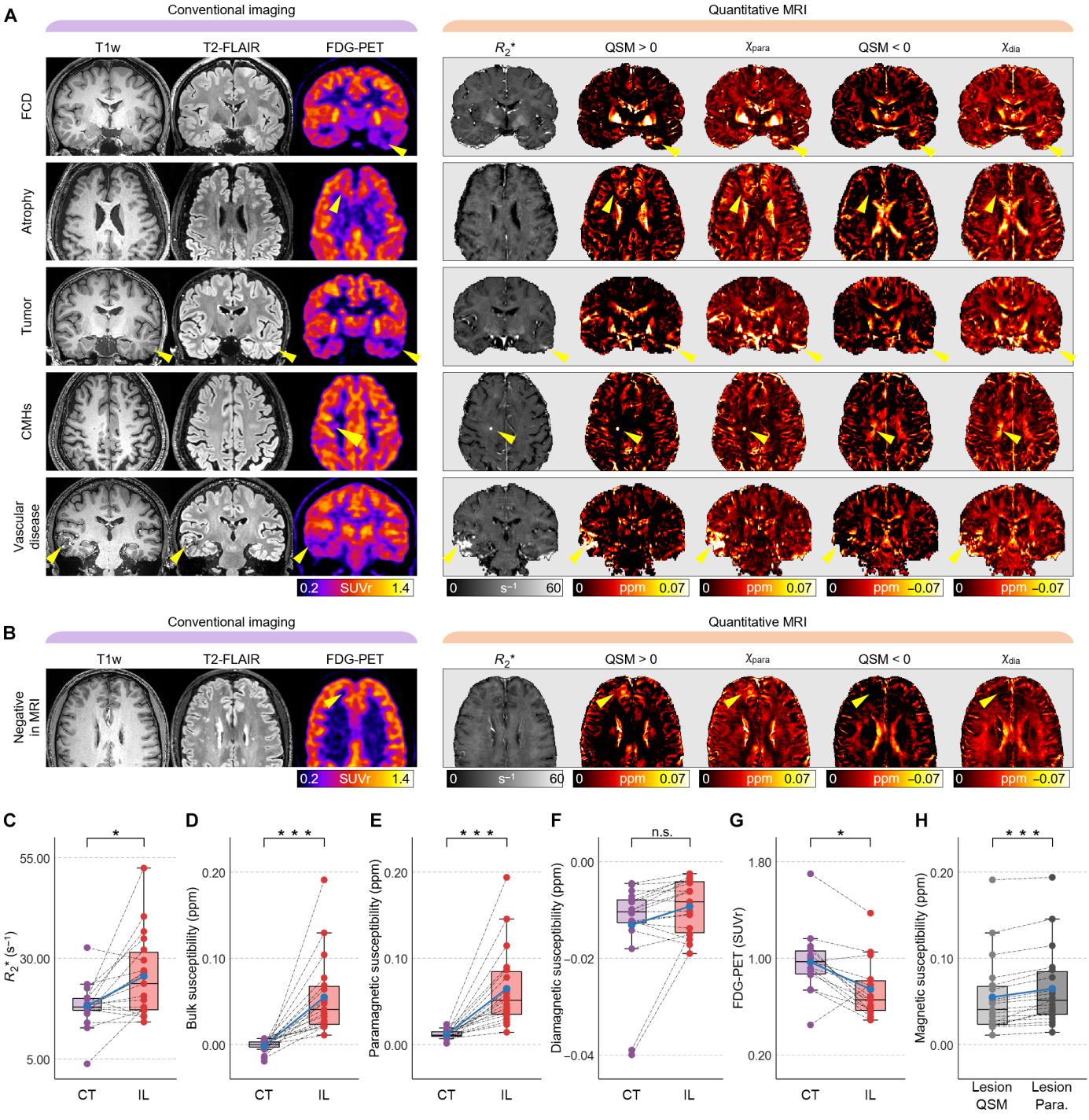

Fig. 1. In vivo imaging of patients with epilepsy and diverse etiologies. (**A**) MRI and FDG-PET imaging were used to detect epileptogenic zones in patients with epilepsy and known etiologies, as identified by conventional MRI. Hyperparamagnetic susceptibility in χ_{para} maps was observed in these zones, accompanied by low ^{18}F-FDG uptake in FDG-PET images. (**B**) For patients with conventional MRI–negative epilepsy, χ_{para} maps detected the epileptogenic zone in the frontal lobe, showing hyperparamagnetic susceptibility consistent with low ^{18}F-FDG uptake in the FDG-PET image. (**C** to **G**) Statistical comparisons were conducted between epileptogenic zones and corresponding contralateral tissues for MRI quantifications (n = 19), including R_2* (C), bulk susceptibility (D), paramagnetic susceptibility (E), diamagnetic susceptibility (F), and FDG-PET (G) (n = 15); n.s., nonsignificant; *P < 0.05 and ***P < 0.001 by paired t test. (**H**) Paramagnetic susceptibility exhibits higher values compared to the corresponding QSM. All statistical analyses were performed with Bonferroni correction. CT, contralateral tissues; IL, ipsilateral lesions; Para., paramagnetic susceptibility.

cannot differentiate between increases in paramagnetic substances or decreases in diamagnetic substances, limiting their specificity for quantification. In addition, they often underestimate overall brain susceptibility. In contrast, χ_{para} maps specifically represent iron-dominated paramagnetic substance concentrations, potentially indicating iron overload. Diamagnetic susceptibility (χ_{dia}) can vary depending on the condition. It may decrease in cases such as FCD and atrophy or increase in conditions like vascular diseases and cerebral microhemorrhages (CMHs). In patients with conventional MRI-visible lesions, such as those with cases of tumors or vascular disease (Fig. 1A, bottom two rows), all imaging modalities revealed epileptogenic zones. The χ_{para} maps showed ultrahigh paramagnetic susceptibility compared to the contralateral normal tissues, suggesting iron overload because of hemorrhage or vascularization. For a proportion of patients without visible lesions on structural MRI images or R_2* or QSM maps, hyperparamagnetic susceptibilities were observed (Fig. 1B), identifying epileptogenic zones along with low ^{18}F-FDG uptake. More structural MRI-negative patients with hyper-χ_{para} are provided in fig. S1B. This indicates that the iron-sensitive χ_{para} maps effectively expand the detection capabilities of MRI.

Paramagnetic susceptibility combined with diamagnetic susceptibility distinguishes different subtypes of epilepsy

The epileptogenic zones were not always associated with iron overload. A proportion of patients (11 of 156, 7.1%) exhibited abnormal susceptibility patterns without showing hyper-χ_{para} (classified as non–hyper-χ_{para}). These patterns included hypo-χ_{para} combined with either hypo-χ_{dia} or hyper-χ_{dia}, as well as normal χ_{para} paired with hyper-χ_{dia} (fig. S1A and table S1).

One representative patient, who had undergone resection and was diagnosed with FCD IIb (patient no. 9), presented an epileptogenic zone characterized by both hypo-χ_{para} and hypo-χ_{dia}. This pattern suggested reduced iron levels accompanied by demyelination (fig. S2B). Both paramagnetic and diamagnetic susceptibilities revealed a disruption of the normal layer-specific structure, as indicated by yellow and blue arrows. Approximately 2.0% of patients in our cohort (3 of 156) exhibited these magnetic characteristics (table S1). In addition, a subset of patients (6 of 156, 3.9%) showed hypo-χ_{para} with hyper-χ_{dia}, indicating decreased iron levels with calcification. A smaller proportion of patients (2/156, 1.3%) displayed hyper-χ_{dia} alone, indicative of calcification or zinc deposition.

In contrast, QSM was unable to separately quantify the paramagnetic and diamagnetic components of susceptibility (fig. S1A), limiting its ability to identify specific tissue composition changes. This limitation highlights the importance of using methods that can distinguish between these two types of magnetic susceptibilities to better understand the underlying pathological processes in epilepsy.

Quantifying iron overload in epileptogenic zones using paramagnetic susceptibility

To further illustrate the quantitative capability of χ_{para}, we analyzed the epileptogenic zones in patients who underwent resection surgery. Contralateral normal tissues were identified by mirroring the corresponding lesions. Potential iron overload was confirmed in 19 patients by the significantly increased R_2* (Fig. 1C, $P = 0.045$), bulk susceptibility (Fig. 1D, $P < 0.001$), and χ_{para} (Fig. 1E, $P < 0.001$) in the lesions. The χ_{dia} showed only slight changes (Fig. 1F). FDG-PET images were acquired for 15 of these patients, revealing significantly reduced ^{18}F-FDG uptake in the lesions (Fig. 1G, $P = 0.014$). The χ_{para} shows generally higher values than the QSM in lesioned tissues (Fig. 1H), suggesting potential diamagnetic substances removed from bulk susceptibility. In addition, similar distributions of QSM and χ_{para} indicated demyelination in lesioned tissues.

Linear analysis between FDG-PET and MRI-based quantification is shown in Fig. 2 (A to D). The iron-sensitive χ_{para} showed a significant linear correlation with ^{18}F-FDG uptake rates (Fig. 2C, $P = 0.034$). Similar to χ_{para}, QSM exhibited a comparable pattern in regression analysis with FDG-PET, while there is an increase in susceptibility values potentially because of demyelination. However, this increase does not reach statistical significance. The separated χ_{para} and χ_{dia} were not linearly correlated (Fig. 2E). This suggests that iron overload in epilepsy is not fully associated with diamagnetic substances such as myelin and calcium. These observations highlight that iron-quantification capabilities of conventional R_2* and QSM can be biased and influenced by χ_{dia}. In contrast, paramagnetic susceptibility independently quantified iron overload in epileptogenic zones, offering a reliable indicator of the severity of the condition.

Hyperparamagnetic susceptibility observed from the epileptogenic cortex to white matter

In the case of epilepsy caused by traumatic or hemorrhagic incidents, the epileptogenic zones typically correspond to areas with increased χ_{para} at the locations of trauma or bleeding. For other etiologies, hyperparamagnetic susceptibility is consistent with regions of low ^{18}F-FDG uptake in the cerebral cortex. To further assess the extent of iron overload, whole-brain χ_{para} and FDG-PET images were projected onto depth-wise surfaces from the pial surface to the gray matter-white matter (GM-WM) boundary in the cortex, extending into the WM (Fig. 3A). We further collected 14 specimens with various etiologies and conducted ex vivo experiments on resected tissues from localized epileptogenic zones (figs. S2 and S3). Detailed demographic information for the corresponding patients is provided in Table 2. In addition, the information about other patients who underwent resection surgery but did not have their tissues collected is available in table S3.

Representative quantitative maps of depth-wise surfaces from one patient (FCD IIb, patient no. 8) are shown in Fig. 3B. The typical epileptogenic zone was identified at the left temporal pole, where χ_{para} and FDG-PET showed significant changes compared to the contralateral area, suggesting different indications of the lesion. Both maps maintained their variations across all surfaces. The increased χ_{para} showed a more localized characteristic, peaking near the GM-WM boundary. To verify these in vivo imaging observations, we reconstructed the high-resolution χ_{para} map (isotropic resolution of 100 μm by 100 μm by 100 μm) of the specimens (Fig. 3C). Visual inspection revealed an obvious hyperparamagnetic susceptibility band near the GM-WM boundary [superficial white matter (SWM), blue dashed lines in Fig. 3C]. This band, with $\chi_{para} = 0.033 \pm 0.008$ parts per million (ppm), showed higher iron concentration than the normal-appearing (NA) SWM band, which had $\chi_{para} = 0.014 \pm 0.006$ ppm, suggesting abnormal iron deposition in specific microstructures on and beneath the cortex. This finding was further verified across all specimens with increased χ_{para}, where the lesioned SWM showed an average χ_{para} of 0.029 ± 0.009 ppm, while the NA SWM had an average χ_{para} of 0.017 ± 0.006 ppm (fig. S4).

Validation of paramagnetic susceptibility in vivo by LA-ICP-TOF-MS

To further validate the accuracy of quantitative paramagnetic susceptibility imaging for in vivo iron quantification, we measured iron

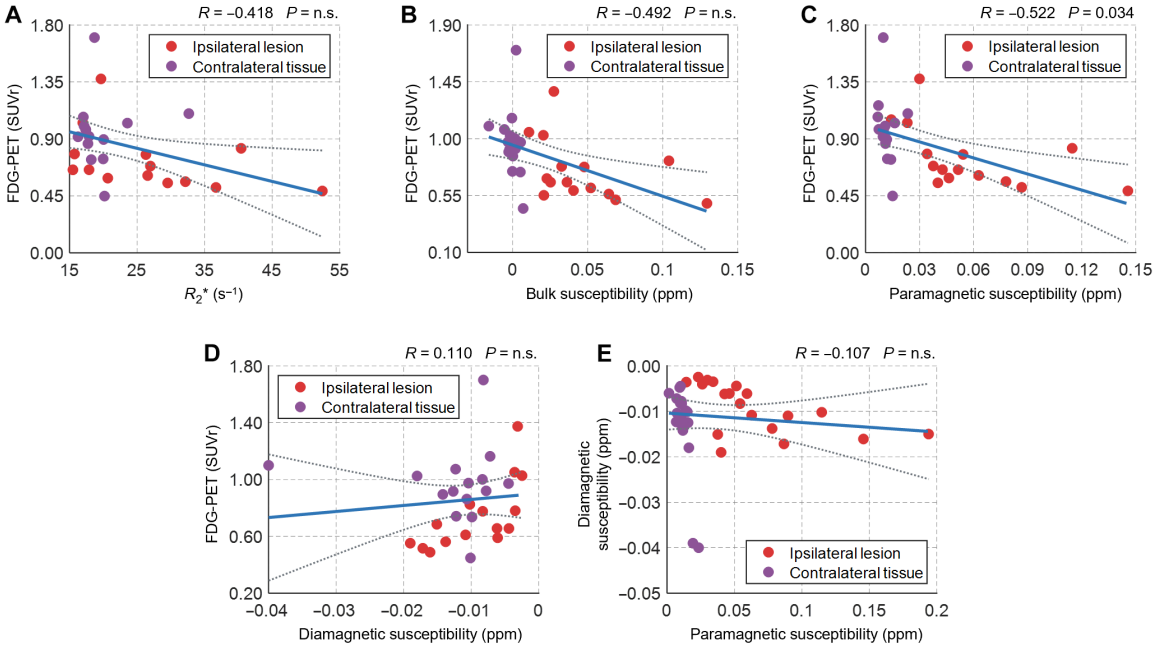

Fig. 2. Linear regression analysis between various imaging quantifications in patients who underwent resection with hyper-χ_{para}. (**A** to **D**) Linear regression analysis of FDG-PET and other MRI quantifications ($n = 15$), including R_2* (A), diamagnetic susceptibility bulk susceptibility (B), paramagnetic susceptibility (C), and diamagnetic susceptibility (D). The area between the two dashed curves represents 95% confidence intervals. Paramagnetic susceptibility showed a linear correlation with ^{18}F-FDG uptake. (**E**) No linear correlation was found between paramagnetic and diamagnetic susceptibility in either epileptogenic zones or contralateral tissues ($n = 19$). All statistical analyses were performed with Bonferroni correction.

concentration (using isotope ^{57}Fe) by laser ablation-inductively coupled plasma time-of-flight mass spectrometry (LA-ICP-TOF-MS) (Fig. 3D and fig. S2). As expected, the iron map revealed a pattern consistent with the ex vivo χ_{para} findings in the epileptogenic zones. A significant linear correlation was found between χ_{para} and iron concentration (Fig. 3E, correlation coefficient $R = 0.582$, $P < 0.001$) and was verified in other specimens (fig. S5). Further iron staining (Fig. 3F) showed a similar pattern of iron overload concentrated in cell-like structures, confirming the accuracy of the iron source detected by χ_{para} (Fig. 3, C and D, white arrows). The specific lesion location identified by the in vivo χ_{para} (Fig. 3G) was precisely matched with the ex vivo χ_{para} map. The corresponding in vivo χ_{dia} map revealed a decrease in iron-overloaded tissues, indicating potential demyelination within the epileptogenic zones. However, the T1-w image was unable to visually identify the lesioned area because of inadequate contrast. To assess the accuracy of iron concentration measurements by quantitative paramagnetic susceptibility imaging in vivo, we extracted six regions of interest (ROIs) covering both lesioned and NA tissues. Linear correlation analysis of ROI-averaged in vivo χ_{para} and iron concentration for each ROI showed a high correlation (fig. S6, D to I, correlation coefficient $R > 0.800$ in all patients) and had an averaged $R = 0.601$ (Fig. 3H, $P < 0.001$). These results demonstrated the sensitivity and accuracy of χ_{para} as an in vivo imaging biomarker for iron heterogeneity in epileptogenic zones.

Disruption of the layer-specific structure in iron-overloaded epileptogenic zones

Previous studies have demonstrated a layer-specific distribution of iron concentration from the cortex to the WM (*36*, *37*) and a variable iron pattern in the cortex associated with brain diseases (*38*). To further investigate the disruption of layer-specific iron distribution in the cortex, we analyzed normalized depth-wise profiles of χ_{para} and iron concentration from the cortex into the WM in specimens.

In specimens with iron-overloaded epileptogenic zones, we identified two distinct regions (Fig. 4, A to D): one with NA tissues (A1) and another comprising iron overload tissues (A2). Normal iron profiles were observed in all NA tissues (Fig. 4, E to H), with a peak in the SWM at depths of 100 to 110%, averaging χ_{para} at 0.020 ppm and iron concentration at 38.728 ppm. Other depths in these areas exhibited relatively low χ_{para} levels, consistent with previous studies. In contrast, iron-overloaded areas showed a disrupted depth pattern compared to NA tissues, especially in the SWM, with an averaging χ_{para} at 0.032 ppm and an iron concentration of 66.332 ppm. Furthermore, different subtypes of patients with epilepsy displayed varied patterns of iron deposition. The FCD I specimen showed increased χ_{para} only in the SWM. The FCD IIa specimen demonstrated elevated χ_{para} in the SWM and WM. For the FCD IIb subtype, there was an increase in χ_{para} in the cortex and the SWM. The neuroepithelial tumor (NET) specimen exhibited abnormal χ_{para} throughout the depth profile. In addition, a higher variability in iron concentrations was observed at each measured depth in the iron-overloaded areas compared to NA tissues in FCD IIb and NET cases (Fig. 4, G and H), indicating a nonuniform distribution of iron deposition within the epileptogenic zones of these subtypes. Meanwhile, the depth profiles of χ_{dia} in FCD I and FCD IIa lesioned tissues were similar to those observed in NA tissues (Fig. 4, E and F). A decrease in χ_{dia} was observed in the lesioned tissues of FCD IIb and NET specimens (Fig. 4, G and H), indicating potential demyelination. An increase in χ_{dia} was specifically identified in the lesioned cortex of the NET specimen, which could be attributed to calcification or zinc

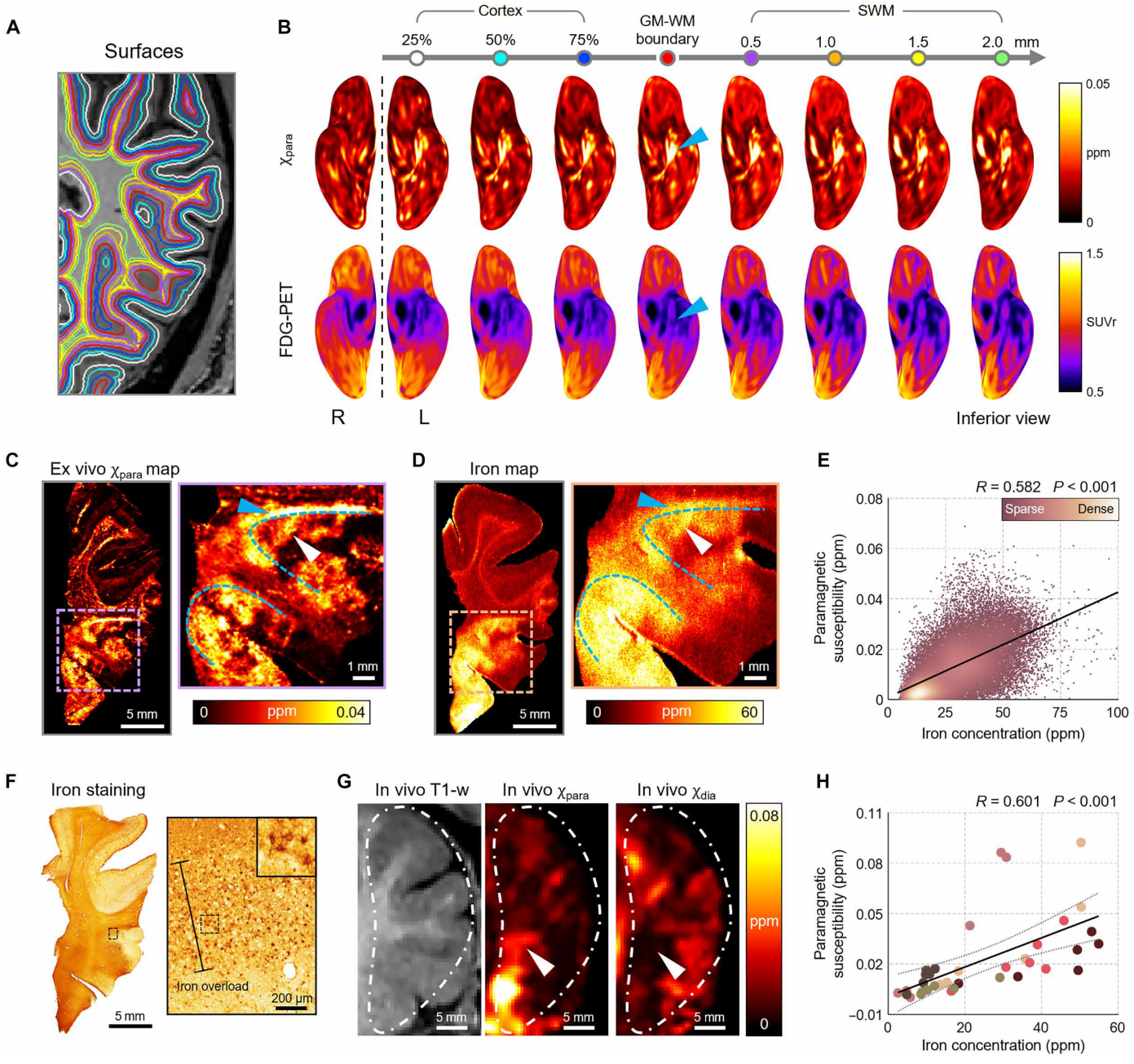

Fig. 3. The χ_{para} map obtained from subvoxel QSM imaging can accurately reveal and quantify iron deposition heterogeneity in epileptogenic zones in vivo. (**A**) Depth-wise surfaces overlaid on T1-w images. (**B**) Depth-wise χ_{para} and FDG-PET surfaces extracted from the cortex (percentage depth) to the SWM. Regions of hyperparamagnetic susceptibility and low SUVr values colocalize in the left temporal pole, identifying epileptogenic zones. (**C**) Ex vivo χ_{para} maps of the specimen from the same region as in (B). (**D**) Iron mass spectrometry results from the same slice shown in (C), revealing iron overload in zoomed-in areas. (**E**) Voxel-wise linear regression between ex vivo χ_{para} (C) and iron concentration (D), showing a strong linear correlation. (**F**) Iron staining results indicate that the observed iron overload is likely localized within cells. (**G**) Precise location of the specimen in the patient's MR image. The in vivo χ_{para} maps effectively quantify excess iron in epileptogenic zones, corroborating findings from the ex vivo χ_{para} maps (C) and iron maps (D). The in vivo χ_{dia} maps exhibit a decrease in the epileptogenic zones, indicating potential demyelination. (**H**) Linear correlation between ROI-averaged χ_{para} and iron concentration across 36 total ROIs (6 ROIs per patient, $n = 6$; data from the same patient are plotted with the same color). The area between the two dashed curves represents 95% confidence intervals in (H).

Table 2. Demographics for patients undergoing surgery with specimen collection. The epileptogenic zones were identified through preoperative radiological assessments using MRI and FDG-PET. MRI evaluations were conducted mainly using T2-FLAIR imaging. A proportion of patients underwent stereoelectroencephalography (SEEG) for more precise lesion localization. The underlying etiology was confirmed through pathological examination. Abbreviations: F, female; M, male; L, left; R, right; B, bilateral; front, frontal lobe; temp, temporal lobe; par, parietal lobe; occ, occipital lobe; amy, amygdala; hip, hippocampus; thal, thalamus; ant, anterior; post, posterior; lat, lateral; ling, lingual; GM, gray matter; WM, white matter; HS, hippocampal sclerosis.

Patient	Sex	Age (year)	Disease duration (year)	Preoperative radiological report				SEEG site	Pathology	Specimen location
				MRI site	MRI report	PET site	PET report			
1	M	24	8	L amy, hip, ant and lat temp	Hyperintensity, blurring	L ant temp, front	Hypometabolism	L front	FCD I	L front
2	M	18	12	R occ	Hyperintensity	R occ	Hypometabolism	R occ	FCD I	R occ
3	M	42	2	R temp	GM-WM blurring, GM thickening	R temp	Hypometabolism	–	FCD IIa	R temp
4	F	37	20	R hip	Hippocampal sclerosis, atrophy	R temp	Hypometabolism	–	FCD IIa	R temp
5	M	5	3	B temp, insula, amy	Hyperintensity	B temp, insula	Hypometabolism	R temp	FCD IIa	R temp
6	F	23	8	L occ	GM-WM blurring, GM thickening	L ling gyrus, occ, B temp	Hypometabolism	L occ	FCD IIa	L occ
7	M	24	22	L temp, insula, hip	Atrophy	L temp, insula, R post insula, temp operculum, ant cingulate	Hypometabolism	L temp	FCD IIa	L temp
				R thal	Hyperintensity, fifth ventricle					
8	M	25	22	L temp pole, hip	Hyperintensity	L temp pole, ant temp	Hypometabolism	L temp	FCD IIb	L temp
9	M	8	6	R occ	Hyperintensity	R occ	Hypometabolism	–	FCD IIb	R occ
10	F	12	9	R par	Hyperintensity	R par-occ	Hypometabolism	–	FCD IIb	R par-occ
11	M	53	52	L temp	Hippocampal atrophy	L temp	Hypometabolism	–	HS	L temp
12	F	33	20	R hip	Hippocampal sclerosis, atrophy	R temp	Hypometabolism	–	HS	R temp
13	M	10	10	L temp	Hyperintensity	L temp	Hypometabolism	–	NET (WHO grade 1)	L temp
14	F	20	3	R temp	GM-WM blurring	–	–	R temp	Negative	R temp

deposition. These findings suggest that iron overload disrupts the normal layer-specific structure of the cortex in epileptogenic zones, accompanied by alterations in other diamagnetic substances.

Cellular sources of high iron concentration in cortical epileptogenic zones

The disrupted cortical structure in iron-overloaded epileptogenic zones of FCD IIb and NET patients suggests substantial cellular-level alterations. A previous study has reported that seizure-related iron accumulation originates from CNS cells (*11*). To explore the source of the iron overload visualized by χ_{para}, we performed immunofluorescence and Perls' staining to colocalize CNS cells (including astrocytes, microglia, and neurons) and iron in both FCD IIb and NET specimens.

Perls' staining revealed higher iron content in lesioned areas compared to the surrounding NA tissues (Fig. 5A, FCD IIb specimen). In NA tissues, tufted astrocytes, identified by anti–glial fibrillary acidic protein (GFAP) expression, exhibited extensive branching and dense processes (Fig. 5B). In contrast, astrocytes in lesioned tissues exhibited shorter, less extensive branches, with partial colocalization of iron (Fig. 5B). Microglia, labeled by anti–ionized calcium-binding adapter molecule 1 (Iba1), were sparsely distributed in NA tissues and partially colocalized with iron in the lesioned areas (Fig. 5C). Neurons, identified by anti–β III tubulin (Tuj1), showed clear cell bodies in NA tissues (Fig. 5D). However, neurons in lesioned tissues exhibited abnormal morphology, associated with iron deposition. Similar abnormalities were observed in NET specimens (fig. S7), where astrocytes were found to colocalize with iron deposits, particularly around small blood vessels.

Further statistical analysis was conducted on both FCD IIb and NET cases. Neuroglial proliferation was observed in the lesioned tissues, with a 339% increase in astrocytes (Fig. 5E) and a 196% increase in microglia (Fig. 5F). This proliferation contributed to iron sequestration in cells (Fig. 5, I and J), ultimately leading to iron accumulation. Although neurons did not show an abnormal increase in number, they did sequester iron (Fig. 5K). Our study found that astrocytes were the primary contributors to iron sequestration, having the highest counts and ratio of iron-positive cells in lesioned areas (Fig. 5, H and L). These findings underscore the critical role of CNS cells in excess iron accumulation and metabolism in epilepsy, confirming their contributions to the observed iron overload.

DISCUSSION

In this study, we demonstrated that quantitative paramagnetic susceptibility imaging effectively detects molecular-level iron in normal

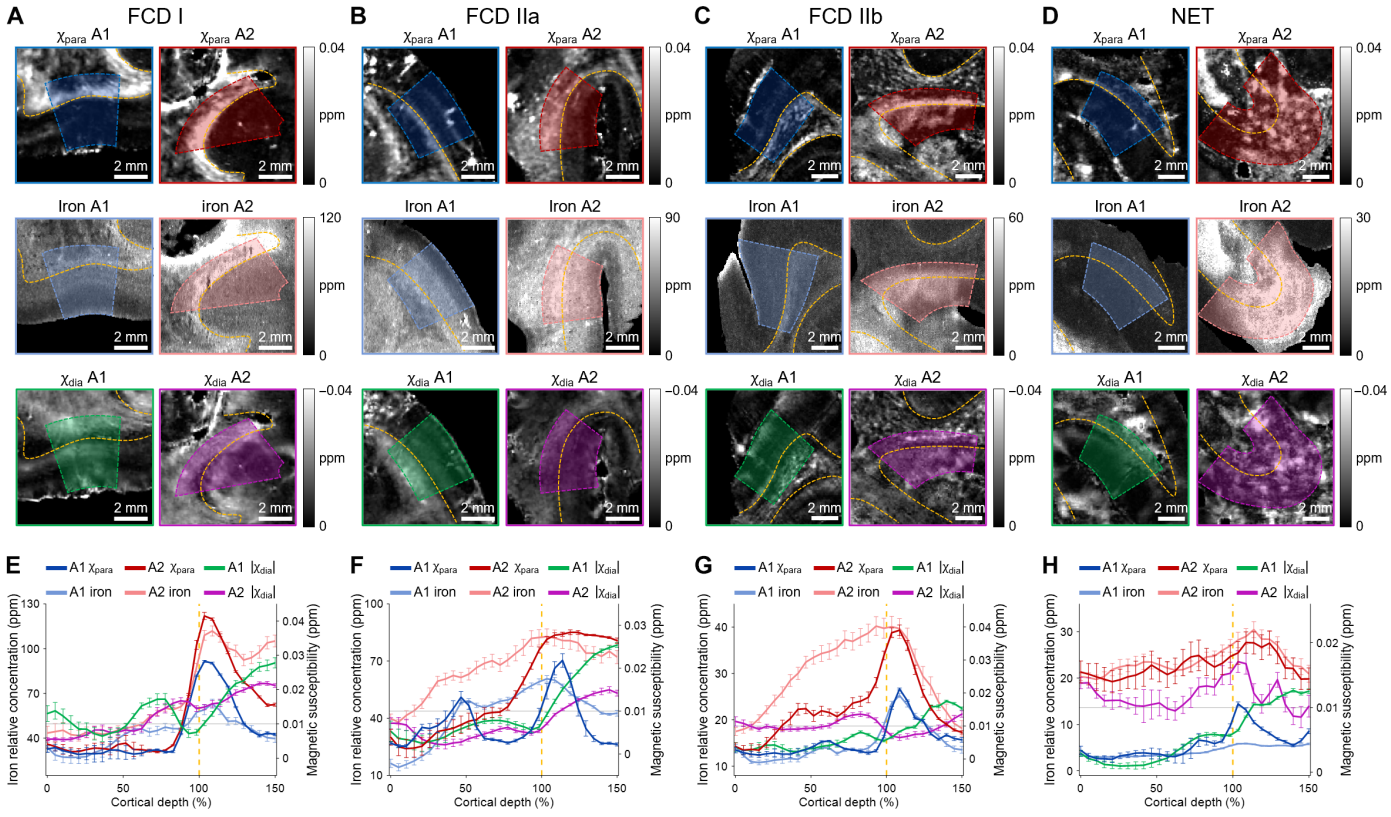

Fig. 4. Depth-wise analysis reveals disruption of the cortical laminar structure in iron-overloaded epileptogenic zones. (**A** to **D**) Two regions (A1 and A2) from each iron-overloaded specimen, representing patients diagnosed with FCD I, FCD IIa, FCD IIb, and NET, were analyzed from the outer cortex to the WM. (**E** to **H**) Normalized depth-wise profiles from the cortical surface (0% depth) through the GM-WM boundary (100% depth) to the WM (150% depth). A reference value of 0.01 ppm (gray lines) was used to compare paramagnetic susceptibility levels across regions of different specimens. The yellow dashed lines at 100% depth represent the GM-WM boundary. Regions with normal iron level (A1) display distinct layer-specific characteristics in χ_{para}, with a peak in the SWM (100 to 110% depth). Corresponding χ_{dia} increases in the WM, reflecting prominent myelination. In contrast, iron-overloaded regions (A2 of each specimen) exhibit notably higher χ_{para} values, with varying patterns depending on the epilepsy subtype. Abnormal χ_{dia} values are also observed in FCD IIb and NET cases (G and H) in A2 regions compared to A1, suggesting changes in diamagnetic substances such as myelin, calcium, or zinc.

tissues and epileptogenic zones in epilepsy. Understanding the complex pathophysiology of epilepsy, which involves various molecular and cellular processes, is crucial for diagnosis, monitoring, and treatment (*39*). Epileptic lesions often involve astrocyte dysregulation, leading to iron accumulation. Excess iron is tightly linked to oxidative stress, which can damage or kill CNS cells (*15*). Measuring iron concentration provides insights into epileptic pathology and cortical changes, but accurately mapping this in vivo has been challenging with existing imaging techniques. Our results show that the specific physical parameter χ_{para} can map tissue iron with a high linear correlation with iron concentration across a wide range in vivo (Fig. 3H). Using χ_{para}, we found that 35.9% (56 of 156) of patients with epilepsy in our cohort with diverse etiologies exhibited iron overload. In addition, iron deficiency was observed in 5.8% (9 of 156) of the patients. Through χ_{dia} assessment, we also detected demyelination or calcification in these subjects. We also detected disruptions in the cortical layer structure from the cortex to the WM using χ_{para} maps both in vivo and ex vivo, indicating dysregulation in CNS cells involved in iron sequestration.

Although iron is known to be ferromagnetic, it behaves as a paramagnetic component in brain tissues, forming compounds such as hemosiderin (Fe^{3+} and Fe^{2+}), deoxyhemoglobin, methemoglobin, or ferritin, essential for brain functions (*40*–*44*). Proper iron regulation is vital to avoid its toxic effects (*45*), which can cause oxidative stress, lipid peroxidation, and ferroptosis, potentially leading to seizures (*45*, *46*). Excess iron is linked to neuronal death and metabolic dysregulation, which can be detected through ^{18}F-FDG uptake in FDG-PET imaging in epileptogenic zones (*15*, *46*). We demonstrated that χ_{para} hyperintensity represents excess iron concentration and reflects reduced metabolic rates in epileptogenic zones (Figs. 2C and 3, C, D, and G). While other paramagnetic substances exist in the brain, such as copper (e.g., Cu^{2+}) (*47*), iron remains the predominant paramagnetic susceptibility source in brain tissues, with the largest molar susceptibility and abundance (*48*). In vivo and ex vivo linear regression analysis (Fig. 3, E and H) indicates that non-iron contributions are negligible compared to the large range of iron-contributed χ_{para}. Therefore, the paramagnetic parameter χ_{para} is an excellent imaging biomarker for tracking epilepsy progression induced because of abnormal iron metabolism.

In contrast to the whole low-metabolic specimens for the surgical resection to prevent a recurrence, excess iron deposition manifests as a more localized characteristic with an area of a small part of sulci or gyri (Fig. 3B). Localized iron deposition disrupts the cerebral cortex's original laminar structure, affecting CNS cell distribution, especially

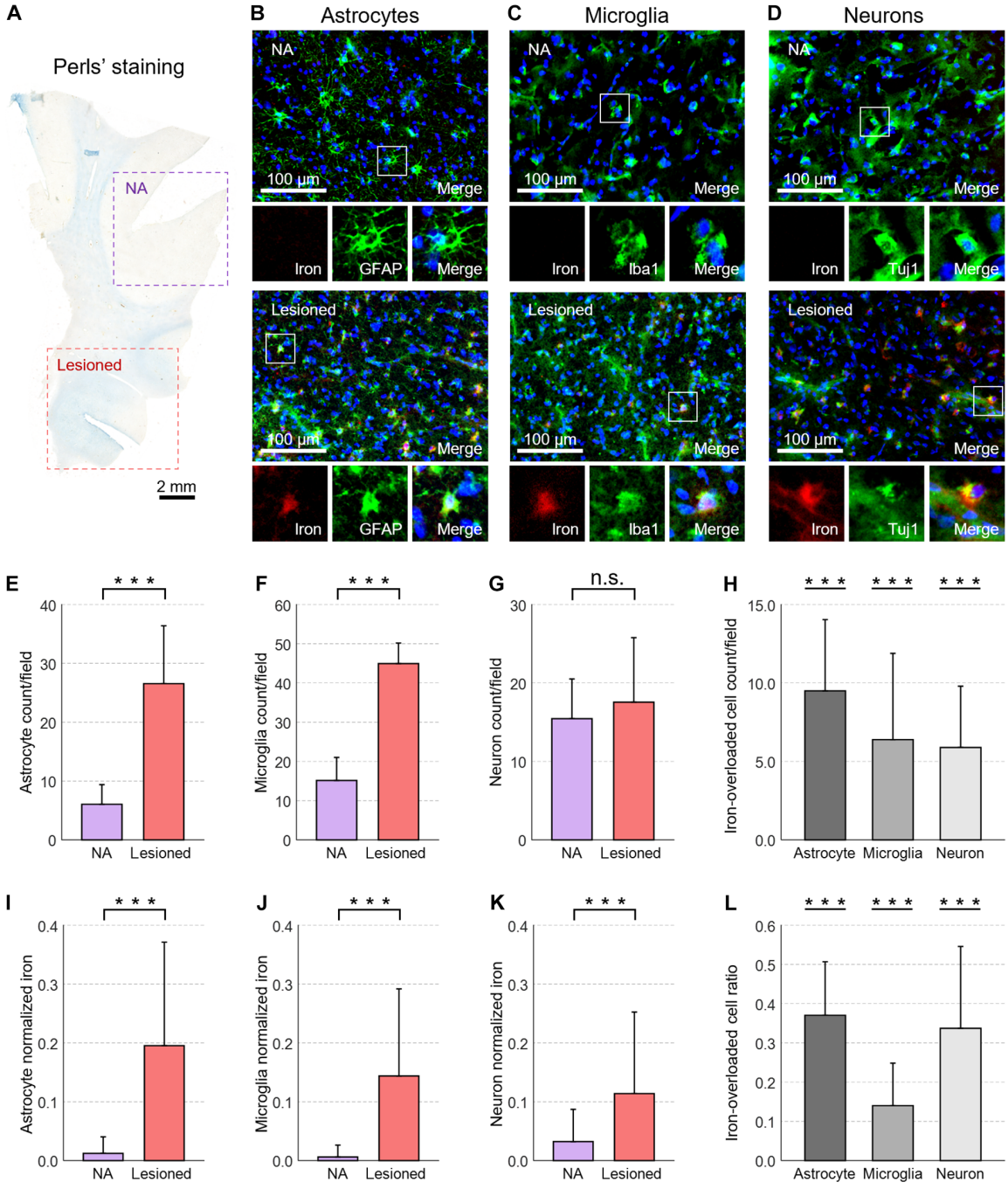

Fig. 5. Iron accumulation in lesioned tissues sequestered within pycnotic astrocytes, microglia, and neurons. (**A**) Perls' staining for iron. (**B**) Iron partially colocalizes with GFAP-labeled astrocytes in lesioned tissues. (**C**) Iron partially colocalizes with Iba1-labeled microglia in lesioned tissues. (**D**) Iron partially colocalizes with Tuj1-labeled neurons in lesioned tissues. (**E** and **F**) Proliferation of astrocytes (E) and microglia (F) in lesioned tissues. (**G**) Counts of neurons in NA and lesioned tissues. (**H** and **L**) Iron-overloaded cells and their ratio in lesioned tissues. A statistical two-sample *t* test was performed between NA and lesioned tissues for each cell type. Iron-overloaded cells and ratios in NA tissues were nearly zero and were not plotted. (**I** to **K**) Normalized iron concentration in NA and lesioned tissues colocalized in each cell type. Two-sample *t* test on normalized iron concentration in NA and lesioned tissues for CNS cells. ***$P < 0.001$.

in the FCD IIb and NET cases (Figs. 4 and 5, A to D, and fig. S7). Our results show that astrocytes and microglia proliferate abnormally and sequester iron in epileptogenic zones from both FCD IIb and NET patients, consistent with previous studies (*11*, *13*). In particular, astrocytes are closely associated with epilepsy and abnormal iron metabolism (*11*). Astrocytes with pycnotic morphology in epileptogenic zones dysregulate iron transport through the permeability-increased blood-brain barrier to brain tissues, thereby resulting in iron absorption and high concentrations of deposition of hemosiderin (*11*, *49*, *50*). We found a high increase in astrogliosis with the most highly overloaded iron sequestration in iron deposition areas (Fig. 5, E and I), and this dysregulation can be specifically detected by χ_{para}. This may indicate that the presence of potentially salvageable tissue in iron-normal NA regions could be identified by χ_{para}. In addition, astrocytes associated with iron influence the occurrence and progression of epilepsy by regulating pro-inflammatory states in the epileptic brain (*51*, *52*).

The origin of iron varies across different epileptic etiologies. Tumors are known to compromise the integrity of the blood-brain barrier (*53*). Iron within tumor tissues may originate from proliferative blood vessels, which penetrate brain tissues and lead to iron accumulation. This, in turn, accelerates ferroptosis (*54*, *55*), a process that can contribute to seizure activity. Our findings corroborate this mechanism (figs. S2A, NET specimen, and S7A). Previous studies have shown that FCD IIb is characterized by oxidative stress, chronic activation of Nrf-2 (nuclear factor erythroid 2–like 2), and disruptions in redox state and iron metabolism, often associated with mammalian target of rapamycin dysregulation and developmental malformations (*11*, *13*). Zimmer *et al.* further demonstrated that early sustained activation of higher lipid peroxidation and dysregulation of iron metabolism are key pathological features of FCD IIb. Our study also confirms that this type of iron deposition can be sequestered by CNS cells. These processes occur before seizure onset and may contribute to epileptogenesis.

Now, surgery remains the most effective treatment of FCD IIb and tumors for patients with epilepsy. However, exploring new drug therapies is crucial for alleviating patient suffering. Evidence suggests that FCD IIb and NET epilepsy, characterized by iron overload, could be mitigated by reducing iron uptake into CNS cells, thereby decreasing their inflammatory state. This approach holds therapeutic promise for epilepsy (*15*, *56*). Zimmer *et al.* proposed that agents inhibiting iron adaptation, such as Nrf-2 inhibitors or ferroptotic agents, could serve as alternative strategies for intervening in aberrant pre-epileptogenic cellular processes (*13*). Other studies have suggested that phosphorylated heat shock protein β-1 may help to reduce iron levels by inhibiting transferrin receptor–1 expression (*57*), potentially preventing the onset of seizures. The efficacy of such therapies could be monitored using quantitative paramagnetic susceptibility imaging, offering a noninvasive means to evaluate treatment outcomes.

Various MRI techniques have been proposed for iron quantification by using magnetic susceptibility, but they face challenges like mixed substance information to the measured susceptibility value (*20*). For example, susceptibility-weighted imaging, combining magnitude and high-frequency phase information of the MRI signal, enhances the susceptibility contrast by magnetic sources (*58*). However, the phase is not an intrinsic tissue property and mixes all the substance information in tissues. The same problem appears in R_2* images, a widely used technique for iron quantification in brain and liver tissues, ignoring the magnitude decay effects by other substances such as myelin or calcium as well as the natural relaxation rate offset (i.e., R_2 relaxation rate) (*59*). QSM techniques were developed by directly decoding the susceptibility information from phase images (*31*), although they must account for coexisting sources like iron, calcium, and myelin.

Lorio *et al.* were the first to systematically explore MRI-based magnetic susceptibility, observing a decrease in iron and myelin in FCD IIb lesions, along with increased calcium, zinc, and iron in glioneuronal tumor cases (*25*). This groundbreaking work in QSM studies on epilepsy pathology has inspired the development of subvoxel QSM methods, enabling more detailed and precise analyses of susceptibility changes in epilepsy. Our study builds on these advancements, showing progress in the application of magnetic susceptibility for studying epilepsy pathology. Specifically, we demonstrated that χ_{para} can effectively quantify iron and the corresponding χ_{dia} was used to quantify myelin, calcium, and zinc. Among the 14 collected specimens, 4 cases (including FCD I, FCD IIa, FCD IIb, and tumor specimens) exhibited iron overload, as indicated by χ_{para}, with demyelination identified through χ_{dia}. In addition, we also observed hypo-χ_{para} susceptibility in another FCD IIb specimen. Our histological studies revealed similar abnormalities in magnetic substances in both FCD IIb and tumor (NET) samples, consistent with findings reported by Lorio *et al.* (fig. S2, A and B).

FCD IIb is characterized by cytoarchitectural alterations, including dysmorphic neurons and balloon cells. In our collected FCD specimens, we observed notable demyelination in FCD IIb cases. Our study shows both iron overload and iron deficiency in these FCD IIb specimens, suggesting two potential pathologic pathways connecting iron and neuronal function. Iron overload is closely associated with cell death, as it catalyzes the Fenton reaction, leading to the production of reactive oxygen species and lipid peroxidation, ultimately resulting in ferroptosis and neurodegeneration within brain tissue (*15*, *16*). Conversely, iron deficiency can lead to reduced myelin synthesis, impaired synaptogenesis, and altered neurotransmitter homeostasis, all of which can compromise neurodevelopment (*46*). This may indicate that increased iron levels have damaged the originally normal nerve fibers, whereas decreased iron levels have prevented the nerve fibers from developing properly. These findings suggest that FCD IIb patients could be categorized on the basis of χ_{para} and χ_{dia} measurements. Specifically, FCD IIb cases could be subdivided into three groups according to whether χ_{para} values are increased, decreased, or normal, potentially indicating distinct underlying pathologies. Future studies are necessary to validate the pathological and radiological values of these maps in larger cohorts. Overall, our findings demonstrate that in vivo χ_{para} and χ_{dia} notably enhance the ability to independently quantify iron and myelin noninvasively. This approach provides a more precise alternative to conventional QSM, which primarily identifies the dominant magnetic source.

In normal brain tissues, iron and myelin are often found to coexist. However, in the lesioned tissues of neurological disorders, including epilepsy, excessive iron can lead to myelin damage. This demyelination can extend to both SWM and WM, which may be detectable through decreased χ_{dia}. It is crucial to acknowledge that substances like zinc and calcium also contribute to χ_{dia}. Our findings show that in lesions with excess iron, diamagnetic calcium and zinc levels increase, coinciding with demyelination. Therefore, myelin quantification using measured χ_{dia} can be influenced by the presence of these diamagnetic ions. Future advancements in subvoxel QSM techniques should focus on

the separated quantification of myelin and diamagnetic ions, especially in evaluating their efficacy for detecting demyelination or calcification in epilepsy (*25*, *26*).

Clinical implementation of paramagnetic susceptibility imaging can be integrated with routine gradient echo sequences without additional costs or time for patients with epilepsy (*60*). For instance, this imaging can complement conventional structural MRI (e.g., T1-w and T2-FLAIR) for detecting morphological changes and iron-related abnormalities in suspected epileptogenic zones (Fig. 1B). The ease of deploying physically informed χ_{para} for iron quantification makes it suitable for major clinical MR scanners. The same principle for iron quantification could potentially be transferred to other iron-related neurodegenerative diseases, such as multiple system atrophy, Alzheimer's disease, progressive supranuclear palsy, Parkinson's disease, and multiple sclerosis (*61*, *62*).

However, this study has some limitations. Nonisotropic acquisition was performed on magnetic susceptibility imaging to balance patient tolerance and susceptibility precision, which may introduce perturbations to the quantification of QSM and subvoxel QSM images (*63*). We conducted ex vivo magnetic susceptibility mapping using a high isotropic resolution, validating the accuracy of paramagnetic susceptibility imaging for quantifying iron in brain tissue. The choice of reference values, which should be carefully selected to ensure accuracy, could also influence MRI-based susceptibility values (*64*). This issue is more commonly encountered in ex vivo magnetic susceptibility measurements, where the lack of a suitable reference tissue can lead to misestimation, which may affect χ_{para} values. Furthermore, follow-up experiments and analysis for patients with epilepsy would be useful to further explore the specificity and sensitivity of χ_{para} in iron quantification.

In summary, we introduced quantitative paramagnetic susceptibility imaging using subvoxel QSM as an imaging biomarker for detecting and quantifying iron concentration in epilepsy in vivo. We found that iron overload is more frequent than iron deficiency in epileptogenic zones localized to more specific cortical regions, disrupting the layer structure, and was sequestered by proliferating CNS cells, particularly astrocytes. Our approach can aid in diagnosing and evaluating iron deposition in patients with epilepsy and has the potential to support personalized therapeutic strategies.

MATERIALS AND METHODS

Participants

All procedures of the current study were approved by the Ethics Committee of Ruijin Hospital Luwan Branch, Shanghai Jiao Tong University School of Medicine (approval no. LWEC2023040). Patients with epilepsy admitted to the hospital's epilepsy center were screened for eligibility. Written informed consent was obtained from all participants or their guardians before the study's initiation. Inclusion criteria for patients entailed a diagnosis of refractory epilepsy without a history of psychiatric disorders or other neurological diseases. Patients were excluded if they had contraindications to 3.0-T MR scanning, such as having a metallic implant, suffering from claustrophobia, or being pregnant. The in vivo imaging data were obtained during patients' initial scans before any intracranial interventions. Relevant clinical data were collected from the patients' electronic medical records. During the study period, 39 participants from the cohort underwent resection surgery following strict clinical protocols.

In vivo imaging acquisition

The MR scanning protocol was performed for each patient at the Ruijin Hospital Luwan Branch using a 3.0-T MRI scanner (uMR890, United Image Healthcare, Shanghai, China) with a 48-channel radio frequency (RF) head coil. The protocol for patients with epilepsy included three-dimensional (3D) inversion recovery–prepared fast spoiled gradient echo sequence for T1-w imaging, inversion recovery spin echo sequence for T2-FLAIR imaging, multiecho gradient echo (mGRE) sequence, and multiecho spin echo (mSE) sequence for quantitative imaging.

The imaging parameters for this study were as follows: T1-w: postinterpolation spatial resolution, 0.5 mm by 0.5 mm by 0.5 mm; repetition time (TR), 7.51 ms; echo time (TE), 3.4 ms; inversion time, 1100 ms; bandwidth (BW), 240 Hz per pixel; flip angle (FA), 15°; total acquisition time (TA), 7 m:5 s. T2-FLAIR: postinterpolation spatial resolution, 0.53 mm by 0.53 mm by 0.53 mm; TR, 6000 ms; TE, 400 ms; inversion time, 1845 ms; BW, 600 Hz per pixel; FA: 66°; TA, 7 m:53 s. Reconstruction with twofold interpolation with artificial intelligence–assisted compressed sensing was applied to the above imaging to acquire higher quality of tissue structural images. mGRE: axial scan; spatial resolution, 1.03 mm by 1.03 mm by 2.00 mm; TR, 35 ms; TE_1/spacing/TE_6, 2.5/4.3/24.0 ms; BW, 350 Hz per pixel; FA, 15°. mSE: spatial resolution, 1.20 mm by 1.20 mm by 2.00 mm; TR, 2900 ms; TE_1/spacing/TE_6, 10.5/10.5/63 ms; BW, 225 Hz per pixel; TA, 7 m:42 s.

All FDG-PET scans were performed at the Shanghai Universal Medical Imaging Diagnostic Center on a Siemens Biograph mMR scanner (Siemens Healthcare, Erlangen, Germany) with an eight-channel phase-array head coil. Patients fasted for 4 to 6 hours and were then intravenously administered ^{18}F-FDG at a mean dose of 0.1 mCi/kg body weight. After 30-min resting, the static PET data were acquired in list mode with a spatial resolution of 1.04 mm by 1.04 mm by 2.03 mm. The list-mode data of the point source were reconstructed using the ordinary Poisson ordered subset expectation maximization algorithm, with eight iterations and 21 subsets, followed by postfiltering with a 2.0-mm full width at half maximum Gaussian kernel. The relative scatter correction was applied, and all FDG-PET images were normalized to the standardized uptake value ratio (SUVr) using the mean cerebellar uptake as the reference.

Magnetic susceptibility map reconstruction

QSM maps were derived by the phase component from mGRE data. Initially, raw phase images underwent unwrapping by a Laplacian-based method (*65*). The brain tissue phase was extracted by varying spherical kernel filtering (V-SHARP) (*66*). The first-echo tissue phase image was discarded because of inadequate phase accumulation (*67*, *68*), which could lead to increased noise levels and a decreased contrast-to-noise ratio (fig. S8). The remaining phase images were averaged across echo times. Last, QSM maps were reconstructed by the streaking artifact reduction method (STAR-QSM) (*69*).

The paramagnetic and diamagnetic susceptibility maps were reconstructed using the APART-QSM method (*35*). Briefly, this subvoxel QSM method introduces a comprehensive complex GRE data model with a voxel-specific magnitude decay kernel (a) to characterize the behaviors of χ_{para} and χ_{dia} in the GRE signal (S) on the basis of given echo time (TE_j) and magnetic field (B_0). Formally, the signal model is given by

$$S(\mathrm{TE}_j) = M_0 e^{-(R_2 + a|\chi_{para}| + a|\chi_{dia}|)\mathrm{TE}_j} \cdot e^{i\{\phi_{res} + 2\pi f_{bg}\mathrm{TE}_j + 2\pi\gamma B_0[D^*(\chi_{para}+\chi_{dia})]\mathrm{TE}_j\}}$$

where M_0 is the extrapolated magnitude signal at zero echo time. $2\pi f_{bg}TE_j$ denotes the background phase. ϕ_{res} represents the residual phase. D is the magnetic dipole kernel, and γ is the gyromagnetic ratio.

Whole-brain R_2 maps were estimated from the mSE data and rigidly registered to the first-echo magnitude image of the mGRE data. Last, the subvoxel QSM maps were generated with the APART-QSM algorithm using the complex GRE data, the QSM maps, and the preregistered R_2 maps. The mGRE-derived R_2* maps were simultaneously estimated using a monoexponential model in the APART-QSM method. All image processes were executed on MATLAB 9.7 (R2019a, MathWorks Inc., Natick, MA). The paramagnetic susceptibility maps from APART-QSM were used to quantify the iron concentration.

In vivo data processing and analysis

Whole-brain image analysis

Before analysis, all the other images were rigidly registered to the individual T1-w structural images. The T1-w images and the T2-FLAIR images, combined with the FDG-PET images, were used for brain dysplasia assessment, metabolic function evaluation, seizure pathogenesis identification, and epileptogenic zone localization. Quantitative MRI images (including the R_2*, QSM, χ_{para}, and χ_{dia}) were used for the tissue characteristics variation analyses in epileptogenic zones. We focused on the hyperparamagnetic susceptibility signals in epileptogenic zones, which may reveal excess iron deposition. Epileptogenic zones were semiautomatically segmented and manually corrected using ITK-SNAP (www.itksnap.org) (*70*). Two experienced neurologists evaluated all MRI and FDG-PET images in consensus.

Statistical analysis

Comparisons of demographic, clinical, and paramagnetic susceptibility characteristics across various pathogenetic groups were conducted using standard statistical tests. Analysis of variance (ANOVA) or chi-square tests were used on the basis of the distributional properties of the data using MATLAB for the analyses. For patients who underwent resection surgery and showed iron overload detected by MRI quantifications, paired sample t tests were conducted to compare ipsilateral lesions with their contralateral tissue counterparts in terms of R_2*, bulk susceptibility, paramagnetic susceptibility, diamagnetic susceptibility, and FDG-PET imaging data. Contralateral tissues were identified by nonlinearly transforming the first-echo magnitude image of the mGRE data to a symmetric T1-w template (ICBM 2009c Nonlinear Symmetric) (*71*). The ipsilateral lesions were then mirrored onto the contralateral hemisphere, followed by inverse transformation to map then back to the individual subject's space. The Bonferroni correction was implemented on all statistical tests, with a corrected $P < 0.05$ as a significant difference. Linear regression analysis was performed between paramagnetic and diamagnetic susceptibility, as well as all MRI quantifications and FDG-PET.

Brain neocortical and subcortical surface mapping

To demonstrate the depth-wise hyperintensity features of paramagnetic susceptibility extending from the cortex to subcortical regions within the epileptogenic zones, the cortical surfaces and WM surfaces were generated using FreeSurfer (http://surfer.nmr.mgh.harvard.edu/). Specifically, individual T1-w images served as the basis for surface reconstruction within FreeSurfer. The depth-wise cortical surfaces were generated at specific distance fractions (25, 50, and 75%) from the pial surface to the GM-WM boundary in the cortex and at constant depths (0.5, 1.0, 1.5, and 2.0 mm) beneath the GM-WM boundary. The paramagnetic susceptibility maps and FDG-PET images were sampled at predefined surfaces and subsequently projected onto the standard FsAverage surface template within FreeSurfer, with spatial smoothing applied using a 6-mm full width at half maximum Gaussian kernel.

Ex vivo specimen preparation and MR measurements

Fourteen blocks of human neocortical tissue specimens of epileptogenic zones were obtained from the epilepsy center at Ruijin Hospital Luwan Branch. These specimens came from drug-resistant patients with epilepsy who underwent surgical resection after a thorough preoperative assessment. The neocortical resection for each patient was tailored on the basis of electrophysiological and imaging data to minimize brain function deficits. On the basis of preoperative in vivo paramagnetic susceptibility maps, four specimens were expected to be iron overloaded, while the others were not. The specimens were fixed in a 4% paraformaldehyde solution immediately after surgery. The entire procedures of patient recruitment, obtaining informed consent, collecting personal data, and the protocol for brain tissue specimen acquisition were all approved by the institutional review board.

Following fixation at 4°C for 4 weeks, the specimens were transferred into 0.01 M phosphate-buffered saline (1× PBS) for an additional week to prepare them for MR scanning by allowing signal recovery.

For MR scanning, the specimens were placed in a 50-ml centrifuge tube and immersed in liquid fluorocarbon (Galden, PFPE, Solvay, Brussels, Belgium). The MRI data were acquired on a 9.4-T MR scanner (Bruker, BioSpec 94/30, Ettlingen, Germany) with a three-channel receive-only RF surface array coil. The specimens were oriented so that their long axes aligned with the main magnetic field. High-resolution 3D mGRE and mSE images were acquired with individually optimized parameters for each specimen, ensuring an isotropic spatial resolution of 100 μm across all specimens. Partial Fourier acquisition was used at a ratio of 0.75 to accelerate the scanning process. The mGRE sequence was acquired with a TR of 250 ms and FA of 45°. For the mSE sequence, the TR was 400 ms. Five to seven echoes were acquired with minimum TE and echo spacing of both sequences.

Histology in epileptogenic zone specimens

Brain tissue preparation

To validate the iron quantification accuracy of the paramagnetic susceptibility map, the same tissue specimens were processed for histochemistry and quantitative iron mapping after completing MRI acquisition. The specimens were cryoprotected in 15 and 30% sucrose at 4°C until the tissue sank. Once sunk, specimens were embedded in an optimal cutting temperature compound (Tissues-Tek, Torrance, US) and stored at −80°C until they were ready for sectioning. The specimens were cut into 50-μm-thick sections with a maximum cross section using a cryostat (Leica CM1950, Wetzlar, Germany). Consecutive sections were washed with 1× PBS for subsequent staining and mass spectrometry analysis.

Immunofluorescence and histochemistry

Tissue sections underwent Perls' staining (Solarbio, Beijing, China) for 20 min at 37°C to delineate the distribution of tissue iron. To improve the bright-field contrast of iron, the staining was enhanced with 3,3′-diaminobenzidine (Solarbio, Beijing, China) for 20 min at 37°C. Whole-section imaging was acquired using an upright microscope (Leica DM6 B, Wetzlar, Germany) at a magnification of 10×. Adjacent sections were immersed in Luxol fast blue for 6 hours at 60°C for myelin staining.

For classifying the distribution of potentially iron-overloaded cell types in the epileptogenic zones, immunofluorescence and Perls' costaining were performed on the same sections. Astrocytes, microglia, and neurons were costained with iron, and pathological changes of cells from normal to lesioned tissues were simultaneously analyzed. Selected sections were washed three times in 1× PBS for 5 min each and then permeabilized in 0.3% Triton X-100 (Sigma-Aldrich, US) for 20 min on a rocking platform at room temperature. Washing steps were repeated, and sections were then blocked with 2% bovine serum albumin (MeilunBio, China) for an hour. Subsequently, sections were incubated overnight (for 16 hours) at 4°C with primary antibodies [Rabbit-anti-GFAP (1:200, Millipore AB5804, US), Rabbit-anti-Iba1 (1:200, Abcam ab178680, UK), and Rabbit-anti-Tuj1 (1:200, Abcam ab52623, UK)]. Following primary incubation and subsequent washes, sections were incubated with the Donkey-anti-Rabbit-IgG-488 secondary antibody (1:500, Invitrogen A21206, US) for an hour in the dark. Sections were then thoroughly washed and incubated with 4′,6-diamidine-2′-phenylindole dihydrochloride (1:1000, Beyotime C1002, China) for 5 min, followed by two more washes for 5 min each. Last, the sections were subjected to Perls' staining procedures. The images were acquired using the same microscope but at a higher magnification of 20× to capture detailed costaining results.

Quantitative elemental mapping with LA-ICP-TOF-MS

Elemental mapping was conducted on sections from every specimen using LA-ICP-TOF-MS. Selected sections underwent continuous ablation in a line-by-line mode using a commercial laser ablation system (NWRImageGeo, ESI, US) at a rapid ablation speed of 12,000 μm/s, a 193-nm laser wavelength, a rectangular laser spot size of 60 μm by 60 μm, and a repetition frequency of 200 Hz. Energy fluence was calibrated to 0.6 J/cm^2 to completely ablate the 50-μm tissue layer without contamination from the underlying glass substrate. The ablated tissues were transported to an inductively coupled plasma time-of-flight mass spectrometer (TOFWERK ICPTOF R, TOFWERK, Switzerland) via a helium gas stream at a flow rate of 0.244 liters/min. Upon ablation, tissue ionization was achieved through an RF plasma source operational at 1400 W. Argon was used as the plasma, auxiliary, and transport gas with respective flow rates of 15, 1, and 0.9 liters/min. Mass spectra were acquired continuously at a mass resolution of 3000 m/Δm and temporally averaged to a sampling interval of 0.005 s per pixel. The isotope ^{57}Fe was chosen for iron analysis to avoid interference from ^{40}Ar^{16}O during the ablation process, which could affect the naturally abundant isotope ^{56}Fe. The isotopes ^{31}P, ^{44}Ca, and ^{66}Zn were simultaneously acquired as references for diamagnetic susceptibility imaging.

Measured element intensity time profiles of inductively coupled plasma mass spectrometry were converted to 2D maps and processed using Iolite version 4 (Melbourne, Australia). The relative quantitative data (in parts per million) for each point on the LA-ICP-TOF-MS images were obtained by using NIST1486 as a calibration standard.

Ex vivo data processing and statistical analysis

Registration and regression analysis

Paramagnetic susceptibility maps of specimens were semiautomatically linearly registered to the corresponding LA-ICP-TOF-MS (^{57}Fe, iron) images. For the registration between ex vivo χ_{para} maps and iron images, an initial alignment was achieved by manually locating a coarse reoriented paramagnetic susceptibility imaging slice on the basis of the section position of the specimen. This was followed by a linear registration from the 3D resliced ex vivo χ_{para} maps to the 2D iron section images. Voxel-wise linear regression analysis was conducted between ex vivo χ_{para} maps and iron images.

A similar pipeline was applied to in vivo imaging. Tissue blocks were manually labeled and reoriented on T1-w and magnitude images, guided by the preoperative localization of the epileptogenic zones. Linear registration was then performed to align the in vivo tissue block T1-w and magnitude images with the ex vivo magnitude images. Subsequently, this transformation was applied to the in vivo paramagnetic susceptibility imaging data. Given the predefined transformation from ex vivo MRI to iron imaging, a connection was established between in vivo MRI and iron imaging. Given notable resolution differences between in vivo MRI and iron imaging, ROI-averaged linear regression analysis was conducted between iron images and in vivo χ_{para} maps using an ROI with a size of 2.5 mm by 2.5 mm (fig. S4). In total, 36 ROIs (six from each of the six patients) were extracted from the iron images and in vivo χ_{para} maps.

Depth-wise profile generation

Depth-wise cortical-subcortical profiles of paramagnetic susceptibility maps and iron images were produced by averaging values across selected regions. Iron-overloaded regions were identified in four specimens, while NA tissues with a normal iron concentration were extracted from the same specimens. Given the variable thickness of the cortex, each depth-wise profile was converted to percentiles from the pial surface (0% depth) to the GM-WM boundary (100% depth). For plotting the WM profile, the 50% depth of cortical thickness was extended beneath the cortex at that point. These depth-wise profiles were generated using LayNii version 2.3.0 (*72*). The equivolume principle (*73*) was applied to preserve the relative volume across cortical folds, enabling the transformation of values associated with cortical layers of varying thicknesses into standardized depth locations. The final depth-wise profiles consisted of 30 points along the depth, averaged from 60 samples along the GM-WM boundary within the extracted regions.

Statistical analysis

For costaining experiments of CNS cells (astrocytes, microglia, and neurons) and iron, cell counts were conducted in both NA and lesioned tissues within each field of view of 200 μm by 200 μm. In addition, the number of iron-overloaded cells was also recorded. The iron concentration colocalized with each cell type was semiquantified by measuring the normalized iron intensity in bright-field imaging, enabling the comparison of iron sequestration by cells between NA and lesioned tissues. Two-sample *t* tests were performed to compare NA and lesioned tissues regarding CNS cell counts, the number and ratio of iron-overloaded CNS cells, and iron content within CNS cells.

Supplementary Materials

This PDF file includes:

Figs. S1 to S8

Tables S1 to S3

REFERENCES AND NOTES

1. T. A. Milligan, Epilepsy: A clinical overview. *Am. J. Med.* **134**, 840–847 (2021).
2. I. A. W. Kotsopoulos, T. van Merode, F. G. H. Kessels, M. C. T. F. M. de Krom, J. A. Knottnerus, Systematic review and meta-analysis of incidence studies of epilepsy and unprovoked seizures. *Epilepsia* **43**, 1402–1409 (2002).
3. O. Devinsky, A. Vezzani, T. J. O'Brien, N. Jette, I. E. Scheffer, M. de Curtis, P. Perucca, Epilepsy. *Nat. Rev. Dis. Primers.* **4**, 18024 (2018).
4. I. E. Scheffer, S. Berkovic, G. Capovilla, M. B. Connolly, J. French, L. Guilhoto, E. Hirsch, S. Jain, G. W. Mathern, S. L. Moshé, D. R. Nordli, E. Perucca, T. Tomson, S. Wiebe,

Y.-H. Zhang, S. M. Zuberi, ILAE classification of the epilepsies: Position paper of the ILAE commission for classification and terminology. *Epilepsia* **58**, 512–521 (2017).
5. A. Jo, C. Heo, T. H. Schwartz, M. Suh, Nanoscale intracortical iron injection induces chronic epilepsy in rodent. *J. Neurosci. Res.* **92**, 389–397 (2014).
6. Q. Li, Q.-Q. Li, J.-N. Jia, Q.-Y. Sun, H.-H. Zhou, W.-L. Jin, X.-Y. Mao, Baicalein exerts neuroprotective effects in FeCl3-induced posttraumatic epileptic seizures via suppressing ferroptosis. *Front. Pharmacol.* **10**, 638 (2019).
7. P. G. Saletti, I. Ali, P. M. Casillas-Espinosa, B. D. Semple, C. P. Lisgaras, S. L. Moshé, A. S. Galanopoulou, In search of antiepileptogenic treatments for post-traumatic epilepsy. *Neurobiol. Dis.* **123**, 86–99 (2019).
8. L. J. Willmore, J. J. Rubin, Antiperoxidant pretreatment and iron-induced epileptiform discharges in the rat: EEG and histopathologic studies. *Neurology* **31**, 63–69 (1981).
9. L. J. Willmore, G. W. Sypert, J. B. Munson, Recurrent seizures induced by cortical iron injection: A model of posttraumatic epilepsy. *Ann. Neurol.* **4**, 329–336 (1978).
10. L. J. Willmore, Y. Ueda, Posttraumatic epilepsy: Hemorrhage, free radicals and the molecular regulation of glutamate. *Neurochem. Res.* **34**, 688–697 (2008).
11. T. S. Zimmer, B. David, D. W. M. Broekaart, M. Schidlowski, G. Ruffolo, A. Korotkov, N. N. van der Wel, P. C. van Rijen, A. Mühlebner, W. van Hecke, J. C. Baayen, S. Idema, L. François, J. van Eyll, S. Dedeurwaerdere, H. W. Kessels, R. Surges, T. Rüber, J. A. Gorter, J. D. Mills, E. A. van Vliet, E. Aronica, Seizure-mediated iron accumulation and dysregulated iron metabolism after status epilepticus and in temporal lobe epilepsy. *Acta Neuropathol.* **142**, 729–759 (2021).
12. E. A. van Vliet, S. da Costa Araújo, S. Redeker, R. van Schaik, E. Aronica, J. A. Gorter, Blood-brain barrier leakage may lead to progression of temporal lobe epilepsy. *Brain* **130**, 521–534 (2006).
13. T. S. Zimmer, G. Ciriminna, A. Arena, J. J. Anink, A. Korotkov, F. E. Jansen, W. van Hecke, W. G. Spliet, P. C. van Rijen, J. C. Baayen, S. Idema, N. R. Rensing, M. Wong, J. D. Mills, E. A. van Vliet, E. Aronica, Chronic activation of anti-oxidant pathways and iron accumulation in epileptogenic malformations. *Neuropathol. Appl. Neurobiol.* **46**, 546–563 (2020).
14. E. Aronica, K. Boer, A. Becker, S. Redeker, W. G. M. Spliet, P. C. van Rijen, F. Wittink, T. Breit, W. J. Wadman, F. H. Lopes da Silva, D. Troost, J. A. Gorter, Gene expression profile analysis of epilepsy-associated gangliogliomas. *Neuroscience* **151**, 272–292 (2008).
15. S. Chen, Y. Chen, Y. Zhang, X. Kuang, Y. Liu, M. Guo, L. Ma, D. Zhang, Q. Li, Iron metabolism and ferroptosis in epilepsy. *Front. Neurosci.* **14**, 601193 (2020).
16. Y. Cai, Z. Yang, Ferroptosis and its role in epilepsy. *Front. Cell. Neurosci.* **15**, 696889 (2021).
17. P. R. Angelova, N. Esteras, A. Y. Abramov, Mitochondria and lipid peroxidation in the mechanism of neurodegeneration: Finding ways for prevention. *Med. Res. Rev.* **41**, 770–784 (2021).
18. Z. Zhang, W. Liao, B. Bernhardt, Z. Wang, K. Sun, F. Yang, Y. Liu, G. Lu, Brain iron redistribution in mesial temporal lobe epilepsy: A susceptibility-weighted magnetic resonance imaging study. *BMC Neurosci.* **15**, 117 (2014).
19. E.-J. Shin, J. H. Jeong, C. K. Chung, D.-J. Kim, M.-B. Wie, E. S. Park, Y. H. Chung, Y. Nam, T.-V. Tran, S. Y. Lee, H.-J. Kim, W.-Y. Ong, H.-C. Kim, Ceruloplasmin is an endogenous protectant against kainate neurotoxicity. *Free Radic. Bio. Med.* **84**, 355–372 (2015).
20. K. Ghassaban, S. Liu, C. Jiang, E. M. Haacke, Quantifying iron content in magnetic resonance imaging. *Neuroimage* **187**, 77–92 (2019).
21. J. F. Schenck, The role of magnetic susceptibility in magnetic resonance imaging: MRI magnetic compatibility of the first and second kinds. *Med. Phys.* **23**, 815–850 (1996).
22. K. Shmueli, J. A. de Zwart, P. van Gelderen, T.-Q. Li, S. J. Dodd, J. H. Duyn, Magnetic susceptibility mapping of brain tissue in vivo using MRI phase data. *Magn. Reson. Med.* **62**, 1510–1522 (2009).
23. T. Liu, P. Spincemaille, L. de Rochefort, B. Kressler, Y. Wang, Calculation of susceptibility through multiple orientation sampling (COSMOS): A method for conditioning the inverse problem from measured magnetic field map to susceptibility source image in MRI *Magn. Reson. Med.* **61**, 196–204 (2009).
24. M. Aggarwal, X. Li, O. Gröhn, A. Sierra, Nuclei-specific deposits of iron and calcium in the rat thalamus after status epilepticus revealed with quantitative susceptibility mapping (QSM). *J. Magn. Reson. Imaging* **47**, 554–564 (2017).
25. S. Lorio, J. Sedlacik, P.-W. So, H. G. Parkes, R. Gunny, U. Löbel, Y.-F. Li, O. Ogunbiyi, T. Mistry, E. Dixon, S. Adler, J. H. Cross, T. Baldeweg, T. S. Jacques, K. Shmueli, D. W. Carmichael, Quantitative MRI susceptibility mapping reveals cortical signatures of changes in iron, calcium and zinc in malformations of cortical development in children with drug-resistant epilepsy. *Neuroimage* **238**, 118102 (2021).
26. O. C. Kiersnowski, G. P. Winston, L. Caciagli, E. Biondetti, M. Elbadri, S. Buck, J. S. Duncan, J. S. Thornton, K. Shmueli, S. B. Vos, Quantitative susceptibility mapping identifies hippocampal and other subcortical grey matter tissue composition changes in temporal lobe epilepsy. *Hum. Brain Mapp.* **44**, 5047–5064 (2023).
27. G. Xu, X. Chen, Y. Zhang, Quantitative susceptibility mapping shows lower brain iron content in children with childhood epilepsy with centrotemporal spikes. *Jpn. J. Radiol.* **41**, 1344–1350 (2023).
28. D. A. Yablonskiy, E. M. Haacke, Theory of NMR signal behavior in magnetically inhomogeneous tissues: The static dephasing regime. *Magn. Reson. Med.* **32**, 749–763 (1994).
29. J. H. Duyn, J. Schenck, Contributions to magnetic susceptibility of brain tissue. *NMR Biomed.* **30**, 10.1002/nbm.3546 (2017).
30. C. Stüber, M. Morawski, A. Schäfer, C. Labadie, M. Wähnert, C. Leuze, M. Streicher, N. Barapatre, K. Reimann, S. Geyer, D. Spemann, R. Turner, Myelin and iron concentration in the human brain: A quantitative study of MRI contrast. *Neuroimage* **93**, 95–106 (2014).
31. A. Deistung, F. Schweser, J. R. Reichenbach, Overview of quantitative susceptibility mapping. *NMR Biomed.* **30**, 10.1002/nbm.3569 (2017).
32. E. M. Haacke, S. Liu, S. Buch, W. Zheng, D. Wu, Y. Ye, Quantitative susceptibility mapping: Current status and future directions. *Magn. Reson. Imaging* **33**, 1–25 (2015).
33. H. G. Shin, J. Lee, Y. H. Yun, S. H. Yoo, J. Jang, S.-H. Oh, Y. Nam, S. Jung, S. Kim, M. Fukunaga, W. Kim, H. J. Choi, J. Lee, χ-separation: Magnetic susceptibility source separation toward iron and myelin mapping in the brain. *Neuroimage* **240**, 118371 (2021).
34. J. Chen, N. J. Gong, K. T. Chaim, M. C. G. Otaduy, C. Liu, Decompose quantitative susceptibility mapping (QSM) to sub-voxel diamagnetic and paramagnetic components based on gradient-echo MRI data. *Neuroimage* **242**, 118477 (2021).
35. Z. Li, R. Feng, Q. Liu, J. Feng, G. Lao, M. Zhang, J. Li, Y. Zhang, H. Wei, APART-QSM: An improved sub-voxel quantitative susceptibility mapping for susceptibility source separation using an iterative data fitting method. *Neuroimage* **274**, 120148 (2023).
36. M. Fukunaga, T. Q. Li, P. van Gelderen, J. A. de Zwart, K. Shmueli, B. Yao, J. Lee, D. Maric, M. A. Aronova, G. Zhang, R. D. Leapman, J. F. Schenck, H. Merkle, J. H. Duyn, Layer-specific variation of iron content in cerebral cortex as a source of MRI contrast. *Proc. Natl. Acad. Sci. U.S.A.* **107**, 3834–3839 (2010).
37. E. Kirilina, S. Helbling, M. Morawski, K. Pine, K. Reimann, S. Jankuhn, J. Dinse, A. Deistung, J. R. Reichenbach, R. Trampel, S. Geyer, L. Müller, N. Jakubowski, T. Arendt, P.-L. Bazin, N. Weiskopf, Superficial white matter imaging: Contrast mechanisms and whole-brain in vivo mapping. *Sci. Adv.* **6**, eaaz9281 (2020).
38. M. Bulk, W. M. Abdelmoula, H. Geut, W. Wiarda, I. Ronen, J. Dijkstra, L. van der Weerd, Quantitative MRI and laser ablation-inductively coupled plasma-mass spectrometry imaging of iron in the frontal cortex of healthy controls and Alzheimer's disease patients. *Neuroimage* **215**, 116808 (2020).
39. A. Vezzani, T. Ravizza, P. Bedner, E. Aronica, C. Steinhäuser, D. Boison, Astrocytes in the initiation and progression of epilepsy. *Nat. Rev. Neurol.* **18**, 707–722 (2022).
40. C. Liu, W. Li, K. A. Tong, K. W. Yeom, S. Kuzminski, Susceptibility-weighted imaging and quantitative susceptibility mapping in the brain. *J. Magn. Reson. Imaging* **42**, 23–41 (2015).
41. C. D. Coryell, F. Stitt, L. Pauling, The magnetic properties and structure of ferrihemoglobin (methemoglobin) and some of its compounds. *J. Am. Chem. Soc.* **59**, 633–642 (1937).
42. D. S. Taylor, C. D. Coryell, The magnetic susceptibility of the iron in ferrohemoglobin. *J. Am. Chem. Soc.* **60**, 1177–1181 (1938).
43. L. Michaelis, C. D. Coryell, S. Granick, Ferritin: III. The magnetic properties of ferritin and some other colloidal ferric compounds. *J. Biol. Chem.* **148**, 463–480 (1943).
44. T. A. Rouault, Iron metabolism in the CNS: Implications for neurodegenerative diseases. *Nat. Rev. Neurosci.* **14**, 551–564 (2013).
45. J. M. C. Gutteridge, B. Halliwell, Mini-Review: Oxidative stress, redox stress or redox success? *Biochem. Biophys. Res. Commun.* **502**, 183–186 (2018).
46. S. Levi, M. Ripamonti, A. S. Moro, A. Cozzi, Iron imbalance in neurodegeneration. *Mol. Psychiatry* **29**, 1139–1152 (2024).
47. I. F. Scheiber, J. F. B. Mercer, R. Dringen, Metabolism and functions of copper in brain. *Prog. Neurobiol.* **116**, 33–57 (2014).
48. D. R. Lide, "Magnetic susceptibility of the elements and inorganic compounds," in *Handbook of Chemistry and Physics* (CRC Press, ed. 81, 2000), pp. 130–135.
49. L. You, P. P. Yu, T. Dong, W. Guo, S. Chang, B. Zheng, Y. Ci, F. Wang, P. Yu, G. Gao, Y.-Z. Chang, Astrocyte-derived hepcidin controls iron traffic at the blood-brain-barrier via regulating ferroportin 1 of microvascular endothelial cells. *Cell Death Dis.* **13**, 667 (2022).
50. W. Loscher, A. Friedman, Structural, molecular, and functional alterations of the blood-brain barrier during epileptogenesis and epilepsy: A cause, consequence, or both? *Int. J. Mol. Sci.* **21**, 591 (2020).
51. M. Tombini, R. Squitti, F. Cacciapaglia, M. Ventriglia, G. Assenza, A. Benvenga, G. Pellegrino, C. Campana, F. Assenza, M. Siotto, L. Pacifici, A. Afeltra, P. M. Rossini, Inflammation and iron metabolism in adult patients with epilepsy: Does a link exist? *Epilepsy Res.* **107**, 244–252 (2013).
52. P. Sanz, M. A. Garcia-Gimeno, Reactive glia inflammatory signaling pathways and epilepsy. *Int. J. Mol. Sci.* **21**, 4096 (2020).
53. C. D. Arvanitis, G. B. Ferraro, R. K. Jain, The blood–brain barrier and blood–tumour barrier in brain tumours and metastases. *Nat. Rev. Cancer* **20**, 26–41 (2019).
54. A. R. Bogdan, M. Miyazawa, K. Hashimoto, Y. Tsuji, Regulators of iron homeostasis: New players in metabolism, cell death, and disease. *Trends Biochem. Sci.* **41**, 274–286 (2016).
55. Y. Zhao, Y. Liu, Y. Xu, K. Li, L. Zhou, H. Qiao, Q. Xu, J. Zhao, The role of ferroptosis in blood–brain barrier injury. *Cell. Mol. Neurobiol.* **43**, 223–236 (2023).

56. N. Singh, S. Haldar, A. K. Tripathi, K. Horback, J. Wong, D. Sharma, A. Beserra, S. Suda, C. Anbalagan, S. Dev, C. K. Mukhopadhyay, A. Singh, Brain iron homeostasis: From molecular mechanisms to clinical significance and therapeutic opportunities. *Antioxid. Redox Signal.* **20**, 1324–1363 (2014).
57. X. Sun, Z. Ou, M. Xie, R. Kang, Y. Fan, X. Niu, H. Wang, L. Cao, D. Tang, HSPB1 as a novel regulator of ferroptotic cancer cell death. *Oncogene* **34**, 5617–5625 (2015).
58. E. M. Haacke, Y. Xu, Y. C. Cheng, J. R. Reichenbach, Susceptibility weighted imaging (SWI). *Magn. Reson. Med.* **52**, 612–618 (2004).
59. C. Langkammer, N. Krebs, W. Goessler, E. Scheurer, F. Ebner, K. Yen, F. Fazekas, S. Ropele, Quantitative MR imaging of brain iron: A postmortem validation study. *Radiology* **257**, 455–462 (2010).
60. G. Lao, Q. Liu, Z. Li, X. Guan, X. Xu, Y. Zhang, H. Wei, Sub-voxel quantitative susceptibility mapping for assessing whole-brain magnetic susceptibility from ages 4 to 80. *Hum. Brain Mapp.* **44**, 5953–5971 (2023).
61. S. Lee, G. G. Kovacs, The irony of iron: The element with diverse influence on neurodegenerative diseases. *Int. J. Mol. Sci.* **25**, 4269 (2024).
62. S. Hametner, I. Wimmer, L. Haider, S. Pfeifenbring, W. Brück, H. Lassmann, Iron and neurodegeneration in the multiple sclerosis brain. *Ann. Neurol.* **74**, 848–861 (2013).
63. A. Karsa, S. Punwani, K. Shmueli, The effect of low resolution and coverage on the accuracy of susceptibility mapping. *Magn. Reson. Med.* **81**, 1833–1848 (2018).
64. Z. Liu, P. Spincemaille, Y. Yao, Y. Zhang, Y. Wang, MEDI+0: Morphology enabled dipole inversion with automatic uniform cerebrospinal fluid zero reference for quantitative susceptibility mapping. *Magn. Reson. Med.* **79**, 2795–2803 (2018).
65. M. A. Schofield, Y. Zhu, Fast phase unwrapping algorithm for interferometric applications. *Opt. Lett.* **28**, 1194–1196 (2003).
66. B. Wu, W. Li, A. Guidon, C. Liu, Whole brain susceptibility mapping using compressed sensing. *Magn. Reson. Med.* **67**, 137–147 (2012).
67. E. Biondetti, A. Karsa, D. L. Thomas, K. Shmueli, Investigating the accuracy and precision of TE-dependent versus multi-echo QSM using Laplacian-based methods at 3 T. *Magn. Reson. Med.* **84**, 3040–3053 (2020).
68. M. J. Cronin, N. Wang, K. S. Decker, H. Wei, W. Z. Zhu, C. Liu, Exploring the origins of echo-time-dependent quantitative susceptibility mapping (QSM) measurements in healthy tissue and cerebral microbleeds. *Neuroimage* **149**, 98–113 (2017).
69. H. Wei, R. Dibb, Y. Zhou, Y. Sun, J. Xu, N. Wang, C. Liu, Streaking artifact reduction for quantitative susceptibility mapping of sources with large dynamic range. *NMR Biomed.* **28**, 1294–1303 (2015).
70. P. A. Yushkevich, J. Piven, H. C. Hazlett, R. G. Smith, S. Ho, J. C. Gee, G. Gerig, User-guided 3D active contour segmentation of anatomical structures: Significantly improved efficiency and reliability. *Neuroimage* **31**, 1116–1128 (2006).
71. V. Fonov, A. C. Evans, K. Botteron, C. R. Almli, R. McKinstry, D. L. Collins, Brain Development Cooperative Group, Unbiased average age-appropriate atlases for pediatric studies. *Neuroimage* **54**, 313–327 (2011).
72. L. Huber, L. R. Huber, B. A. Poser, P. A. Bandettini, K. Arora, K. Wagstyl, S. Cho, J. Goense, N. Nothnagel, A. T. Morgan, J. van den Hurk, A. K. Müller, R. C. Reynolds, D. R. Glen, R. Goebel, O. F. Gulban, LayNii: A software suite for layer-fMRI. *Neuroimage* **237**, 118091 (2021).
73. J. Consolini, N. Demirci, A. Fulwider, J. J. Hutsler, M. A. Holland, Bok's equi-volume principle: Translation, historical context, and a modern perspective. *Brain Multiphys.* **3**, 100057 (2022).

Acknowledgments: We thank C. Liu at the University of California Berkeley for the helpful discussion. **Funding:** This study was supported by the following: National Natural Science Foundation of China 62471296 (to H.W.), The National Key R&D Program of China (grant 2024YFC2421100) (to H.W.), National Natural Science Foundation of China 62071299 (to Y.Z.), SJTU Trans-med Awards Research STAR 20220103 (to H.W.), and SJTU Trans-med Awards Research YG2023LC02 (to H.W.). **Author contributions:** Conceptualization: Z.L., Q.L., Y.L., F.Y., Y.Z., J.X., and H.W. Methodology: Z.L., Q.L., T.X., M.Z., L.L., Z.C., Y.T., L.J., Y.L., Y.Z., and H.W. Software: Z.L., Q.L., T.X., M.Z., and H.W. Validation: Z.L., Q.L., T.X., M.Z., Y.T., F.Y., Y.Z., and H.W. Formal analysis: Z.L., Q.L., T.X., Y.T., Y.Z., and H.W. Investigation: Z.L., Q.L., M.Z., Y.L., F.Y., Y.Z., and H.W. Resources: Q.L., Y.T., Y.L., F.Y., J.X., and H.W. Data curation: Z.L., Q.L., M.Z., Y.T., L.J., and H.W. Writing—original draft: Z.L., Q.L., Y.L., Y.Z., and H.W. Writing—review and editing: Z.L., Q.L., T.X., M.Z., Y.T., L.J., Y.L., F.Y., Y.Z., J.X., and H.W. Visualization: Z.L., T.X., Y.T., L.J., Y.Z., and H.W. Supervision: Y.T., Y.L., F.Y., Y.Z., J.X., and H.W. Project administration: Z.L., Q.L., Y.T., J.X., and H.W. Funding acquisition: Y.L. and H.W. **Competing interests:** The authors declare that they have no competing interests. **Data and materials availability:** The reconstruction code is available at https://doi.org/10.5281/zenodo.14375619. All data needed to evaluate the conclusions in the paper are present in the paper and/or the Supplementary Materials.

Submitted 30 August 2024
Accepted 14 February 2025
Published 21 March 2025
10.1126/sciadv.ads8149